Materials synthesis in a bubble

Stephan Barcikowski, Anton Plech, Kenneth S. Suslick, and Alfred Vogel

Ultrasonic sonochemistry and pulsed laser ablation in liquids (LAL) are modern techniques for materials synthesis that are in different ways linked to the formation and collapse of cavitation bubbles. We provide an overview of the physics of laser-induced and acoustically driven bubble oscillations and then describe how the high pressures and temperatures associated with ablation and bubble collapse, as well as emitted shock waves, take part in material synthesis inside and around the bubble. Emphasis is placed on the mechanisms of sonochemical synthesis and modification, and on a step-by-step account of the events from laser ablation through interaction of ablation products with the surrounding liquid up to the modification or aggregation of particles within the bubble. Both sonochemistry and LALs yield nanostructured materials and colloidal nanoparticles with unique properties. The synthesis process has been demonstrated to be scalable.

Introduction

The generation and oscillation of transient bubbles in liquids is termed "cavitation." At maximum expansion, the bubble pressure is low and the bubble will collapse due to liquid pressure and surface tension. Important types of cavitation include hydrodynamic, acoustic (e.g., ultrasonic), and laser-induced cavitation.[1–3]

Cavitation phenomena involve a high degree of spatio-temporal energy concentration upon bubble collapse that can result in modifications of adjacent structures (e.g., cavitation erosion). The high pressure and temperature produced upon bubble collapse can also be used for materials processing and synthesis of new materials. In addition, the gas phase of the bubble could contain solid particles and liquid droplets produced by local heating or laser ablation of a solid target immersed in liquid, setting nanoparticles free after collapse. Finally, the shock waves generated by the rebounding of a collapsed bubble[4,5] can have substantial effects on solid particulates suspended nearby in the liquid,[6,7] including fragmentation of friable, brittle materials and agglomeration of malleable ones.[8]

Cavitation erosion is an important feature of hydrodynamic cavitation (e.g., in pumps and propellers) and is associated with the interaction of individual bubbles and bubble clouds with adjacent boundaries.[2,9–11] It has been the historical starting point for intense research on bubble dynamics. Bubble interactions with solid or elastic boundaries generate jetting phenomena arising from the focusing of the liquid flow rushing into the collapsing bubble under aspherical boundary conditions.[1,9,12] Jets concentrate bubble energy at locations away from the bubble center and may thus contribute to material erosion or intended modifications. However, they also transform part of the bubble energy into rotational flow energy, which reduces the collapse pressure and temperature.[9]

The highest pressures and temperatures are observed during spherical bubble dynamics, when the entire bubble energy contributes to the compression of the bubble interior and the surrounding liquid. Spherical bubble oscillations can be induced optically or acoustically. In optical cavitation, tightly focused short laser pulses induce plasma formation at the laser focus ("optical breakdown"[13]) that drives rapid bubble expansion followed by several spherical oscillations.[1,3] In acoustic cavitation, preexisting nuclei are excited by an external sound field.[1] When the frequency of the sound field matches the eigenfrequency of the bubble, resonant excitation produces large bubbles that vigorously collapse, concentrating the ambient acoustic energy by 12 orders of magnitude,[14–16] which produces pressures $>10^3$ MPa and temperatures $>10^4$ K. Thus, spherical collapse may be associated with luminescence and even plasma emission from an optically opaque core—a

Stephan Barcikowski, Technical Chemistry I and Center for Nanointegration Duisburg-Essen, University of Duisburg-Essen, Germany; stephan.barcikowski@uni-due.de
Anton Plech, Institute for Photon Science and Synchrotron Radiation, Karlsruhe Institute of Technology, Germany; anton.plech@kit.edu
Kenneth S. Suslick, Department of Chemistry, University of Illinois at Urbana-Champaign, USA; ksuslick@illinois.edu
Alfred Vogel, Institute of Biomedical Optics, University of Luebeck, Germany; vogel@bmo.uni-luebeck.de
doi:10.1557/mrs.2019.107

phenomenon known as "sonoluminescence."[17–23] The simultaneous generation of high temperature and pressure followed by shock wave emission[5,24,25] provides unique conditions for the induction of chemical reactions (i.e., sonochemistry). While laser-induced cavitation involves single bubbles, sonochemistry generally utilizes cavitation in relatively dense clouds of bubbles and the reactions that occur therein. Here, oscillations of some isolated bubbles will be spherical, but multibubble interaction may also lead to the formation of high velocity liquid jets and turbulent mixing phenomena.[1]

Laser ablation in liquids (LAL) receives great attention[26] because the particles formed are pure (without contaminants from chemical reactants or surfactants), and under appropriate ablation conditions, nanoparticles with monodispersed size distribution can be generated.[27,28] LAL is always associated with cavitation because the phase transition occurring upon ablation produces a rapidly expanding void in the liquid that is filled by the ablation products. The bubble expands beyond its equilibrium radius and collapses again at the surface of the ablation target. Thus, there are two temporal phases of high temperature and pressure that may result in material synthesis and modifications within the bubble—one during ablation and the initial stages of bubble expansion, and a second one upon aspherical collapse and rebound. This results in specific features of material synthesis and modifications that can significantly differ from sonochemistry. In this article, we provide an overview of how the macroscopic hydrodynamics of cavitating bubbles induced by LAL or high-intensity ultrasound interact with and shape the synthesis of new materials and nanostructures.

Physics of laser-induced and acoustically driven bubble oscillations

Laser-induced and isolated acoustically driven bubbles (SBSL) in the bulk of the liquid undergo spherical dynamics if they are small enough not to be affected by buoyancy[29] and when the laser plasma inducing the bubble expansion is sufficiently compact.[3,30] Ultrasonic cavitation involves bubble clouds, and the interaction of neighboring bubbles may result in jetting, which mixes the bubble contents with the surrounding liquid. Jetting phenomena in bubble clouds can be complex because the interaction of adjacent bubbles depends on their distance, relative size, and relative oscillation phase.[31] Complexity is further increased by the interaction with the spatially inhomogeneous sound field. For very small bubbles (i.e., those with maximum radius $R_{max} < 5$ μm), jetting is largely suppressed by the effect of surface tension that increases with decreasing bubble size. Although jetting reduces the collapse pressure, collapse phenomena in

ultrasonic bubble fields were found to be as vigorous as for single-bubble sonoluminescence.[32] This is because there are always bubbles that, at least for some time, are sufficiently isolated to exhibit approximately spherical motion.

For spherically oscillating bubbles produced by optical breakdown in liquids, the pressure transients emitted upon breakdown and collapse have similar amplitude.[4,5] If their initial pressure is sufficiently high, these transients change shape and evolve into shock waves because the speed of sound depends on pressure.[3,33] Pressure amplitudes, p, were determined by measuring the shock wave speed through time-resolved or streak photography (**Figure 1**).[3,24,25,33] The pressure decay as a function of radial (r) propagation distance, $p(r)$, is then deduced using Hugoniot data for water that relate shock pressure to the measured shock wave speed (Figure 1).[3,33] Close to the emission center, p can exceed 10^4 MPa, which implies highly nonlinear propagation with rapid buildup of the shock front and strong dissipation of acoustic energy at the shock front (Figure 1d).[3,34] The dissipated energy can cause significant heating and phase transitions in the liquid medium and alter immersed substances.[35,36] Bubble collapse is associated with emission of blue and UV light, indicative of high temperatures in the bubble interior that may reach up to 20,000 K.[17]

After breakdown, more plasma energy is transformed into shock wave energy than into bubble energy, and upon spherical bubble collapse, most of the energy of the expanded
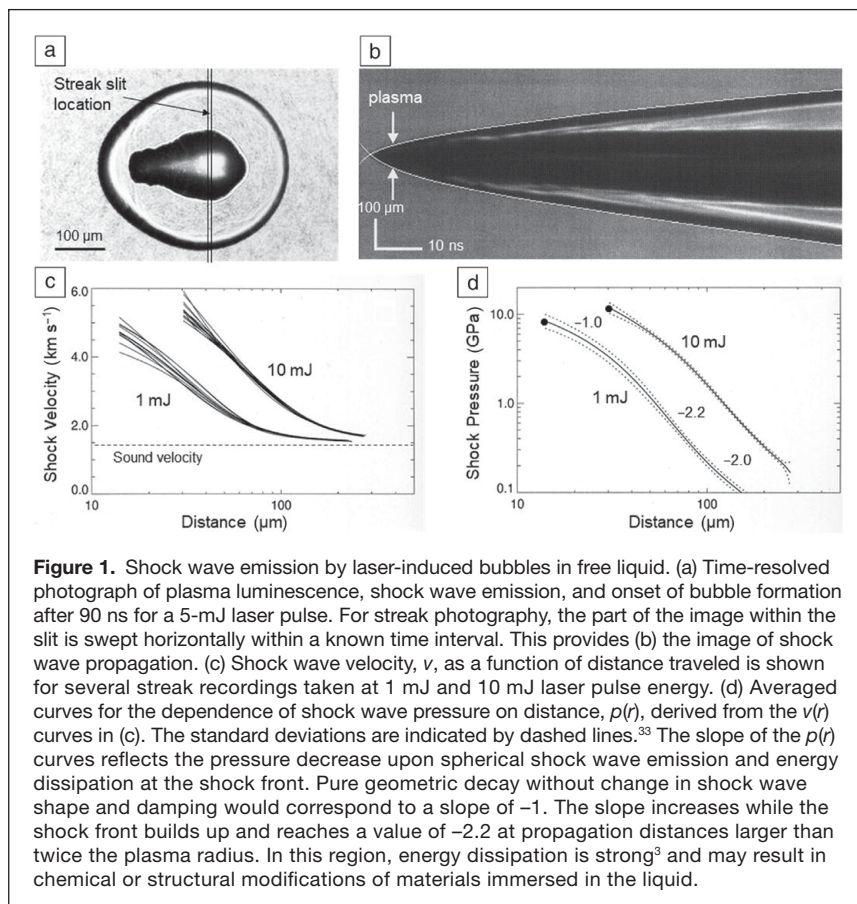

Figure 1. Shock wave emission by laser-induced bubbles in free liquid. (a) Time-resolved photograph of plasma luminescence, shock wave emission, and onset of bubble formation after 90 ns for a 5-mJ laser pulse. For streak photography, the part of the image within the slit is swept horizontally within a known time interval. This provides (b) the image of shock wave propagation. (c) Shock wave velocity, v, as a function of distance traveled is shown for several streak recordings taken at 1 mJ and 10 mJ laser pulse energy. (d) Averaged curves for the dependence of shock wave pressure on distance, $p(r)$, derived from the $v(r)$ curves in (c). The standard deviations are indicated by dashed lines.[33] The slope of the $p(r)$ curves reflects the pressure decrease upon spherical shock wave emission and energy dissipation at the shock front. Pure geometric decay without change in shock wave shape and damping would correspond to a slope of –1. The slope increases while the shock front builds up and reaches a value of –2.2 at propagation distances larger than twice the plasma radius. In this region, energy dissipation is strong[3] and may result in chemical or structural modifications of materials immersed in the liquid.

bubble is radiated away as a shock wave.[4,34,37] Therefore, liquid compressibility must be considered to obtain a realistic picture of the bubble dynamics and its interaction with the surrounding liquid. Spherical bubble dynamics can be described by equations of motion with different degrees of complexity. While the comparatively simple Rayleigh–Plesset equation[1] is suitable for modeling the first bubble oscillation, the Gilmore model (considering the liquid compressibility under pressure) accounts for acoustic energy dissipation and enables tracking the shock wave emission.[1,3] Even more complex bubble models also consider heat and mass transfer at the bubble interface (i.e., vaporization, condensation, and heat conduction).[38,39] While the Gilmore model describes acoustic transient emission utilizing simplifying assumptions based on the conservation of enthalpy, full models are also available, but are far more complex.[38,40,41]

Bubbles around particles

While tightly focused laser pulses can produce bubbles at arbitrary locations in transparent liquids via optical breakdown,[30] bubbles can also be generated by laser irradiation of micro- and nanoparticles. Energy deposition into the particles can be mediated by one-photon absorption of electronic states,[42] resonant plasmonic absorption in metallic nanoparticles,[43–45] or off-resonance irradiation of the metallic particles.[46] In off-resonant excitation, the field enhancement by the particle leads to plasma formation in the surrounding liquid.

Plasmonic nanoparticles offer spatial confinement of thermal effects and bubble-mediated shear damage in biological tissue.[47,48] Antibody-conjugated particles can target specific cells or proteins, and they have been employed for bubble-mediated *in vivo* transfection (transport of nucleic acids across the cell wall).[49,50] Instead of relatively large nanoshells or nanorods,[51] aggregates of smaller particles are an interesting alternative in optoporation (where a transient pore is generated in cell membranes by pulsed laser excitation) and for the transport of therapeutic agents across the cell membrane.[52] Nanoparticle aggregates carrying therapeutic molecules can enter the cell with the help of specific peptides and are enclosed in endosomes. A laser pulse then disrupts the endosomal membrane, whereby the aggregates are released and dispersed inside the cytoplasm. The size of the remaining primary particles is compatible with *in vivo* renal clearance.[52] In contrast to larger particles, which are biopersistent in the body, the smaller primary particles can pass the kidney and be excreted via the urine.

In general, the maximum bubble size extends well beyond the heated zone around the nanoparticle, and the bubble dynamics resemble that of macroscopic bubbles, with an expansion beyond the equilibrium radius and subsequent collapse.[45] However, longer laser pulses produce a sequence of multiple bubble oscillations, with the particle acting as a heat reservoir.[53,54] Thus, the bubble dynamics can be tuned by tailoring size, shape, and optical response of the particles.

Bubble generation and oscillation at a solid boundary

When a bubble oscillates near a solid boundary, the bubble dynamics become aspherical. The flow into the collapsing bubble is impaired by the solid structure, but evolves much faster on the opposite side. It is focused during bubble shrinkage and forms a fast (≈100 m/s) liquid jet, which impinges onto the boundary and can erode it. The process depends strongly on the bubble stand-off distance from the boundary.[1,9,10] Strong jetting requires a finite distance, which is typical for hydrodynamic and ultrasonic cavitation.

In LAL, the bubble is created right at the target surface. On flat targets and for fluids with low viscosity and surface tension coefficient, the bubble assumes an approximately hemispherical shape.[55–58] However, a liquid boundary layer of finite thickness remains at the target surface when the bubble expands beyond the ablation site because the fluid velocity at the surface must be zero (no-slip condition).[59] Therefore, the outer rim of the expanded bubble lifts off from the surface.[55,60,61] Since the bubble wall region with strongest curvature is close to the surface of the solid target, the flow into the cavity is almost radial, and peak pressure and temperature in the collapsed bubble resemble values reached in spherical collapse.[4,9] For LAL in highly viscous fluids, the bubble shape strongly deviates from a hemisphere.[61] The expanding bubble bears a constricted root at the target surface, and its wetting angle cosine reaches values of 0.6. Thus, the bubble shape becomes oblate spheroidal, and the wall region with strongest curvature is located well above the surface.[61] The collapse of an oblate bubble is known to be accompanied by jet formation.[12]

The previously discussed considerations imply that models assuming a perfectly (hemi-)spherical geometry of the expanded bubble[56,62] provide realistic estimates of collapse parameters only when liquid viscosity is negligible. More appropriate are finite-volume methods adapted to the modeling of spherical[41] and aspherical bubble dynamics.[31,41,59,63] Lauterborn and coworkers showed that it is essential to include the expansion phase of laser-induced bubbles into the simulation to obtain realistic bubble shape and collapse dynamics.[64]

First attempts of modeling the collapse of a bubble induced by laser metal ablation in water yielded a temperature of ≈2000 K and a pressure of 380 MPa.[60] However, the simulation started at the stage of maximum bubble expansion and only partially considered the no-slip condition at the boundary. Simulating the dynamics of a bubble attached to a target surface remains a challenge. Experimental data obtained by extrapolating pressure values measured at 10 mm distance to the interior of the collapsed bubble range between 1 and 6 GPa, depending on the stand-off distance of the bubble.[4]

Jet formation upon bubble collapse leads to mixing of the bubble contents with the surrounding liquid. The flow around aspherically collapsing bubbles has been tracked experimentally[9,65–67] as well as by numerical simulations.[31,59,60,63]

Materials synthesis in acoustically collapsing bubbles

For more than two decades, the production of nanostructured materials through the effects of high-intensity ultrasonic irradiation of materials has been a subject of great interest.[8,68–71] Ultrasound in liquids can cause chemical effects over a wide range of size scales, from the mixing and heating of the bulk liquid, to the concentration of energy in microscopic hot spots intense enough to produce high-energy chemical reactions. The wide range of chemical and physical processes caused by ultrasound provides a diverse palette for the formation of nanomaterials with a variety of compositions and structures.

Sonochemistry arises as a consequence of the implosive collapse of bubbles produced by acoustic cavitation,[17] resulting in intense local heating, whose conditions can be determined from the light emitted during cavitation (i.e., sonoluminescence).[23] Spectroscopic studies have shown that these implosions generate temperatures of ~5000 K and pressures >1000 bar (100 MPa) in clouds of cavitating bubbles and even more extreme conditions in isolated single-bubble cavitation.[17–23] The majority of sonochemistry occurs within the heated bubble, but there is also reactivity that comes from an initially liquid phase, primarily from nanodroplets of liquid injected into asymmetrically collapsing bubbles.[22,72] The extremely short time scales of cavitation events and in LALs results in heating and cooling rates of more than 10^{10} K/s of both the bubble vapor[17,72] as well as the inorganic nanoparticles created by LAL.[73,74]

Physical processes arising upon bubble collapse, such as shock wave emission and microjet formation, make ultrasonic irradiation an effective means to mix liquids, erode solid surfaces, and facilitate interparticle collisions among suspended solids in liquids. **Figure 2** provides a general overview of the applications of sonochemical and ultrasonic processes to materials chemistry. Given the space limitations in this article, only a few highlights of the applications of sonochemistry to nanomaterials will be discussed; more thorough discussions can be found elsewhere.[8,68–71]

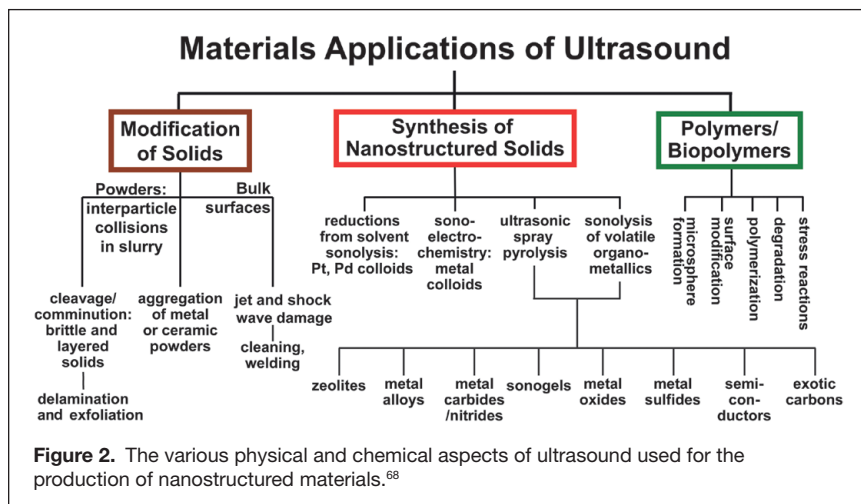### Primary sonochemistry for nanoparticle synthesis

The production of metal nanoparticles from volatile precursors has developed since the first report of amorphous iron nanoparticle synthesis.[75] When a volatile organometallic compound, such as $Fe(CO)_5$, is dissolved in a low-vapor-pressure alkane solvent or ionic liquid[76,77] and subjected to intense ultrasound, the hot spot conditions are sufficient to strip all of the carbonyls from the iron atoms, producing metal nanoparticles. Due to the short lifetime of a cavitation event, the particle is so rapidly cooled during the adiabatic bubble expansion that crystallization is prevented, resulting in amorphous solid particles. The product appears as an agglomeration of 20-nm nanoparticles. If oleic acid or a similar surfactant is added to the reaction mixture, colloidal iron nanoparticles 8 nm in diameter are obtained.[78] Using precursor compounds such as $Fe(CO)_5$ and $Co(CO)_3NO$, amorphous iron, cobalt, and mixed nanoparticles have been made.[79]

The synthesis of amorphous metal nanoparticles can be modified by the addition of other reactants to yield a variety of nanomaterials. Addition of sulfur to a solution of $Mo(CO)_6$ and subsequent sonication produces clustered and agglomerated nanoparticles of MoS_2.[80] This product has a far higher edge surface area than conventionally prepared MoS_2. Since the catalytic activity of MoS_2 is only at the exposed Mo edges, the sonochemically prepared MoS_2 demonstrates much higher catalytic activity for hydrodesulfurization. The sonication of $Mo(CO)_6$ and $W(CO)_6$ dissolved in a hydrocarbon liquid produces molybdenum carbide and tungsten carbide, respectively.[81,82] When these precursors are sonicated in the presence of SiO_2 nanoparticles or other inorganic oxide particles, the catalytic material can be directly deposited onto a support during synthesis.

Secondary sonochemistry for nanoparticle synthesis

Secondary sonochemistry, using a species produced within a cavitating bubble to effect chemical reactions in the liquid phase, is widely employed. Even before the mechanisms of sonochemistry were fully understood, Baigent and Müller showed that ultrasound could be used as an alternative to traditional processes for the production of colloidal gold sols.[83] The sonochemical hot spot generates a variety of radicals (e.g., hydroxyl radicals and hydrogen atoms from water, and alkyl radicals from hydrocarbons) whose secondary reactions can serve as both reductants and oxidants for the production of a wide range of nanoparticles, especially of noble metals.[70]

Sonochemistry has been employed to synthesize a variety of materials other than noble metals with various structures. Among these materials, metal oxide and hydroxide nanoparticles have been produced sonochemically, including MgO,[84] $Sr(OH)_2$,[85] Dy_2O_3,[86] and Fe_3O_4.[87] Metal oxides may be formed through

Figure 2. The various physical and chemical aspects of ultrasound used for the production of nanostructured materials.[68]
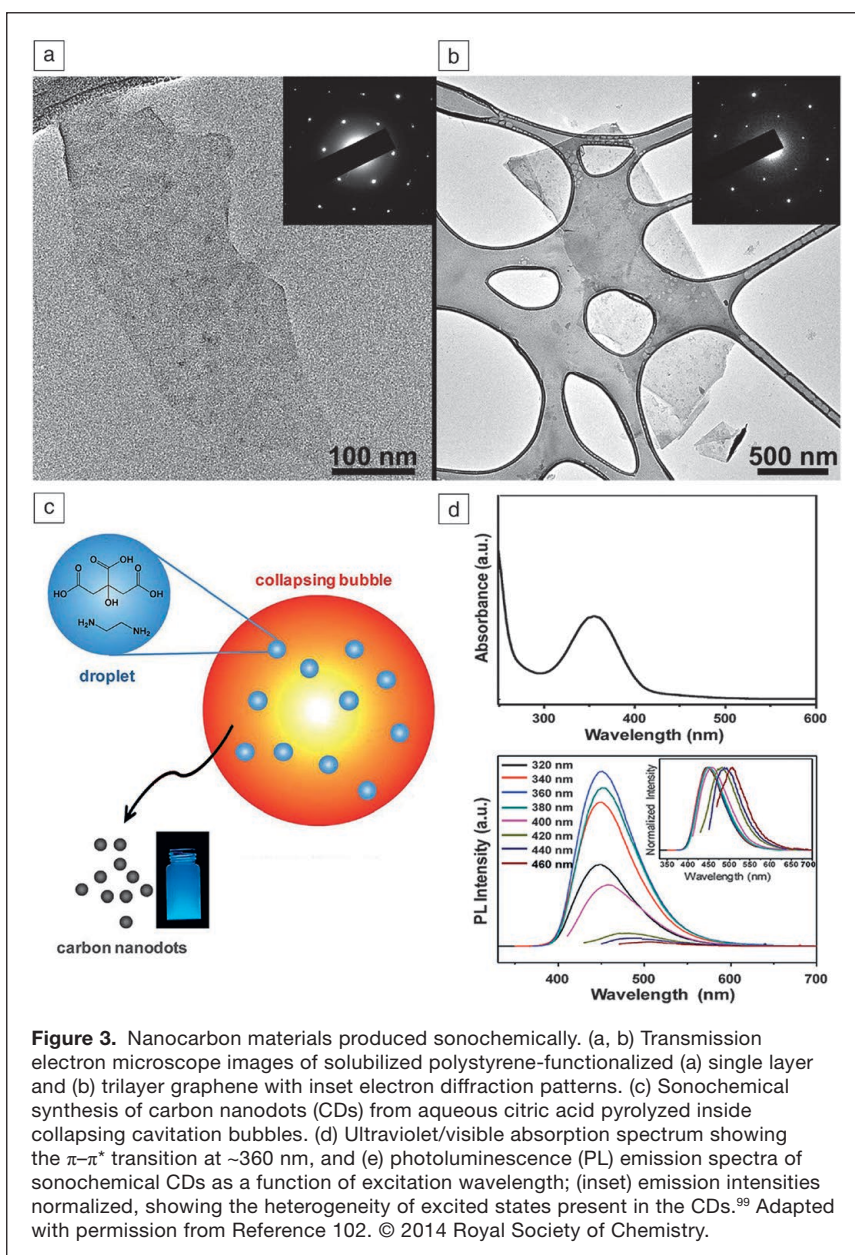
sonochemical oxidation via radicals or through hydrolysis. Nanostructured zinc oxide is a material of interest as a wide bandgap semiconductor, for use as a photocatalyst, and for its antimicrobial properties. Recently, a colloidal suspension of ZnO (10 nm) was produced when $Zn(CH_3CO_2)_2$ was sonicated with a colloidal stabilizer, poly(vinyl alcohol).[88] To make a nanostructured ZnO layer as a matrix in an electrochemical sensor, ZnO nanorods and nanoflakes were grown on a Si substrate by sonicating a zinc salt with hexamethylenetetramine, which served as shape-directing agent.[89] Similarly, ZnO nanoparticles have been sonochemically produced and simultaneously deposited on a textile surface to fabricate an antimicrobial surface in a one-step process.[90] Silver[91] and CuO[92] nanoparticles have also been sonochemically formed on textiles and paper surfaces in a similar manner. The ease of coating a variety of materials with inorganic nanoparticles using ultrasound can be useful for various other applications, especially creating super-omniphobic surfaces.[93]

Skrabalak recently reviewed in detail sonochemical synthesis of high-surface-area carbon materials and nanoparticle depositions.[94] Guo et al. prepared 5-nm TiO_2 nanoparticles deposited on graphene sheets by the ultrasonic irradiation of a suspension of graphene oxide with $TiCl_4$ in ethanol, followed by reduction of the graphene oxide.[95] The composite showed improved activity over TiO_2 alone in the photocatalytic degradation of methylene blue. The authors attribute this improvement in part to the ability of the graphene to reduce the recombination of electron–hole pairs. Sonochemistry has been used to couple graphene oxide and graphene to other nanoparticles, including Au and Fe_3O_4.[96,97] Graphene nanosheets themselves have been produced from the sonochemical reduction of graphene oxide.[98] It was proposed that in addition to dispersing and activating the graphene oxide surface, the radical species produced during cavitational collapse might also play a role in speeding up the reduction of graphene oxide by hydrazine.

Xu and Suslick used sonochemistry to exfoliate graphene directly from graphite and simultaneously functionalize it with polystyrene or poly-4-vinylpyridine to improve its dispersion.[99] As an example, styrene was chosen for graphite exfoliation since it has a surface tension of 35 mN m^{-1}, a good match for graphite's surface energy. Also, under sonochemical conditions, styrene can produce radicals that can chemically attach to the surface of exfoliated graphene sheets and functionalize them, thus improving their dispersibility. This method

produced a colloid of single- and few-layered graphene, as shown in the transmission electron microscopy (TEM) micrograph in **Figure 3**. The polystyrene-functionalized graphene was soluble in a variety of solvents and stable for months without precipitation.

Sonochemistry has been useful in the synthesis of carbon nanotubes. Jeong et al. ultrasonically irradiated a suspension of silica powder in *p*-xylene with a small amount of ferrocene to produce single-walled carbon nanotubes (SWCNTs).[100] The ferrocene decomposed as previously described into amorphous iron particles that were able to catalyze the formation of the SWCNTs, and the *p*-xylene was the carbon source. Recently, Ha and Jeong reported the sonochemical formation of multiwalled carbon nanotubes (MWCNTs) as well.[101]

Figure 3. Nanocarbon materials produced sonochemically. (a, b) Transmission electron microscope images of solubilized polystyrene-functionalized (a) single layer and (b) trilayer graphene with inset electron diffraction patterns. (c) Sonochemical synthesis of carbon nanodots (CDs) from aqueous citric acid pyrolyzed inside collapsing cavitation bubbles. (d) Ultraviolet/visible absorption spectrum showing the π–π* transition at ~360 nm, and (e) photoluminescence (PL) emission spectra of sonochemical CDs as a function of excitation wavelength; (inset) emission intensities normalized, showing the heterogeneity of excited states present in the CDs.[99] Adapted with permission from Reference 102. © 2014 Royal Society of Chemistry.

The sonochemical production of luminescent carbon nanodots (CDs) (Figure 3) by Xu and colleagues demonstrates that the delineation of primary and secondary sonochemistry can be ambiguous.[102] The CDs were made from the sonication of an aqueous solution of citric acid as the carbon source and ethylenediamine as an N-doping source, both in rather high concentration (0.5–1 M). Sonication of the solution for 8 h produced 3–7-nm amorphous particles, as measured by TEM and x-ray diffraction. The CDs had an absorbance band at 354 nm with luminescence at 450 nm. By optimizing the citric acid/ethylenediamine ratio and concentration, particles with quantum yields up to 77% were made, which is high in comparison to other reported CDs.

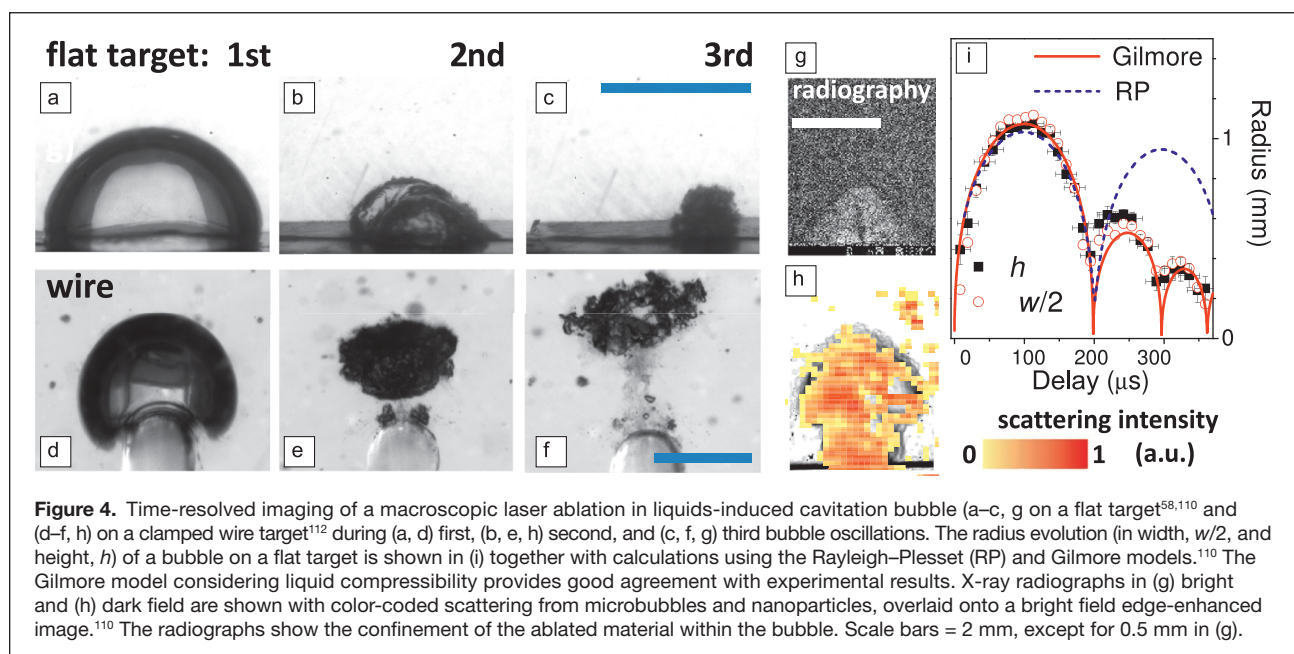## Materials synthesis in bubbles produced by LALs

Pulsed LALs as a colloidal synthesis tool is an emerging field of research[26] for forming nanoparticles with unique properties such as utmost purity[103] or defect richness.[104] The LAL process itself is impressively scalable[105] and even economic,[106] delivering kg throughput of supported catalysts and giving access to the emerging field of additive manufacturing (AM), where polymer[107] and metal[108] powders are decorated with laser-generated nanoparticles to improve the properties of the AM part.

Despite this recent progress demonstrating the colloid's beneficial functionalities, a comprehensive picture of the basic LALs phenomena and nanoparticle (NP) formation mechanisms is still missing. *Ex situ* analysis methods suffer from one problem inherent to the LAL method—the produced NPs are still "alive" after LAL-induced bubble collapse (i.e., they undergo ripening on the seconds-to-days time scale).[109] Advanced analytical *in situ* methods as well as simulations can give access to the missing link in the formation cascade— the synthesis step occurring within the bubble.

The process of LALs is governed by hierarchically inter-related processes, from the atomic and picosecond scale to the macroscopic scale of millimeter-sized bubbles, which complicates strict size control. During ablation, the material is ejected as a mixture of atoms, atom clusters, and liquid droplets.[73] While ablation and most of the molecular modification processes in the ablation plume evolve on a picosecond and nanosecond time scale, the formation and oscillation of a vapor bubble adds a multi-microsecond time scale to the reactions, with the bubble acting as a container for processes modifying the substances produced upon ablation.

Figure 4 shows a range of snapshots for bubble evolution and its relation to the nanoscale material. The bubble dynamics depends on the target geometry. On a large flat target, a nearly hemispherical bubble is formed, and the shape remains during subsequent oscillations.[110] The Rayleigh–Plesset equation[1] is suitable to describe the first oscillation, while modeling of subsequent oscillations requires the consideration of compressibility as provided by the Gilmore model[1] (Figure 4i). Pressure transients produced during collapse and rebound of hemispherical bubbles are in the multi-kilobar range (100s of MPa).[4,9,60] In contrast, asymmetric boundary conditions, such as on curved targets,[111,112] corrugated substrates, or stick-slip motion on the surface,[110] perturb the collapse phase such that pressure transients and the number of oscillations are reduced. Ablation from a wire leads to bubble liftoff before collapse and bubble breakup upon rebound with clouds of microbubbles and ablated nanoparticles (Figure 4f, h).[58,112]

Direct particle detection by time-resolved small-angle x-ray scattering (SAXS) revealed that the vapor bubble is a container for the ablated mass, restricting its dispersion into the liquid medium.[58] Therefore, the collapse reconcentrates the particle mass toward the target. Filaments are sometimes

Figure 4. Time-resolved imaging of a macroscopic laser ablation in liquids-induced cavitation bubble (a–c, g on a flat target[58,110] and (d–f, h) on a clamped wire target[112] during (a, d) first, (b, e, h) second, and (c, f, g) third bubble oscillations. The radius evolution (in width, *w*/2, and height, *h*) of a bubble on a flat target is shown in (i) together with calculations using the Rayleigh–Plesset (RP) and Gilmore models.[110] The Gilmore model considering liquid compressibility provides good agreement with experimental results. X-ray radiographs in (g) bright and (h) dark field are shown with color-coded scattering from microbubbles and nanoparticles, overlaid onto a bright field edge-enhanced image.[110] The radiographs show the confinement of the ablated material within the bubble. Scale bars = 2 mm, except for 0.5 mm in (g).
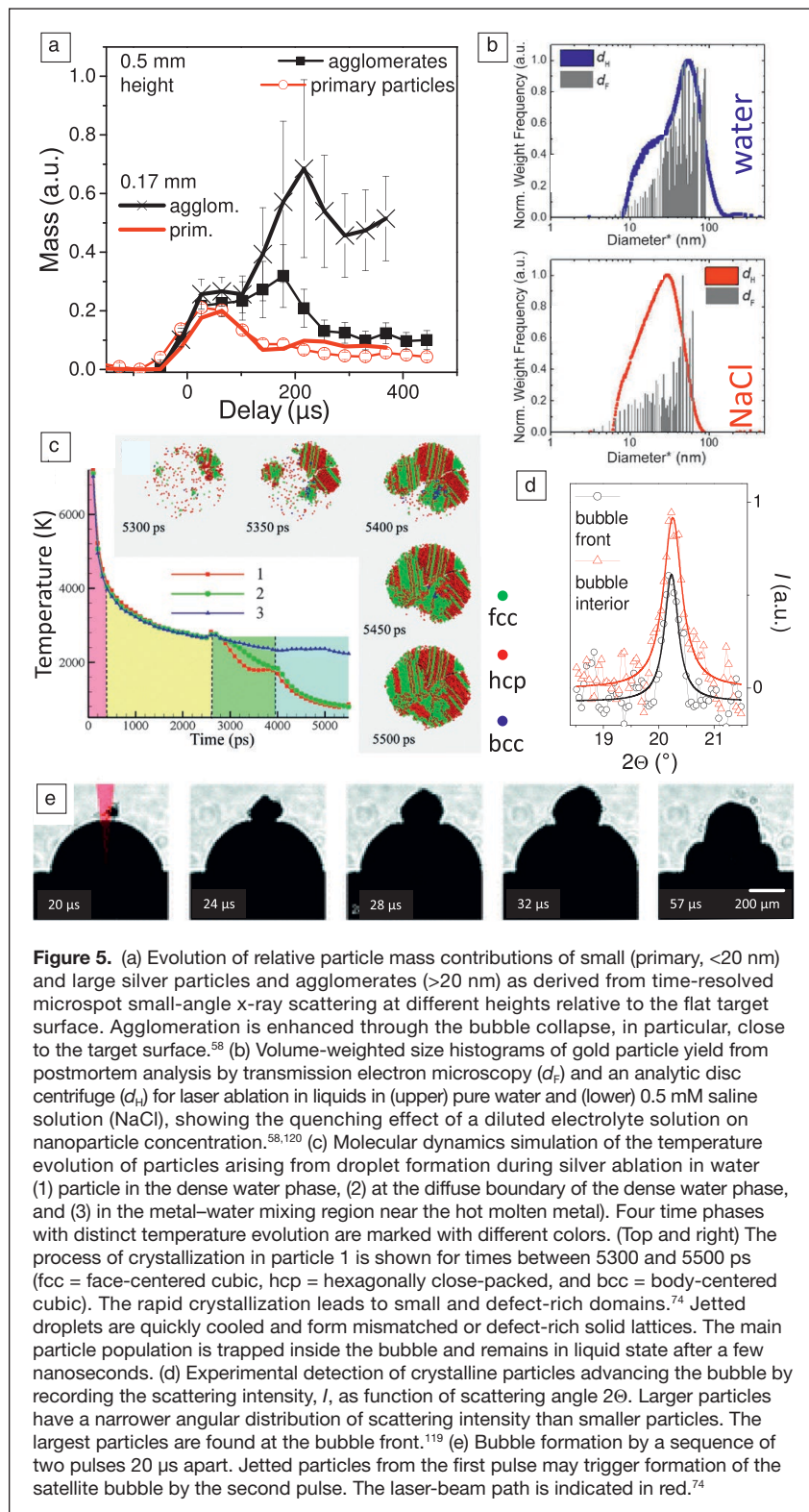
seen inside the bubble by x-ray imaging during its third oscillation (Figure 4g). Concentration and extreme temperature and pressure inside the bubble favor particle aggregation or growth, as can be seen in **Figure 5**a that shows the time evolution of the mass fractions of smaller and larger particles/agglomerates.

One can distinguish between three fractions of ablated material—ultrasmall seeds (i.e., atoms and atom clusters), smaller particles <10 nm, and larger particles (Figure 5b). Atomic-scale simulations linked them to different stages of the ablation process occurring within the first few nanoseconds after a femtosecond or picosecond laser pulse.[73,74,113] Material ablated in the phase explosion regime (i.e., at temperatures beyond the superheat limit) disintegrates into a mixture of vapor and small droplets, when the ablation occurs in vacuum or air.[114] However, in LAL, the ablated material is confined by water and collects at the plume–water interface into a dense superheated molten layer. Water in contact with the hot metal layer is brought into a supercritical state and exerts strong downward pressure on the layer. This rapid deceleration induces nanoscale Rayleigh–Taylor instabilities, which are deformations of an interface between two fluids of different densities that occur when the lighter fluid (the water/vapor) is pushing the heavier fluid (the liquid-metal layer). The instabilities lead to the breakup of the layer into nanoparticles, starting on a time scale of a few nanoseconds and resulting in the formation of particles typically >10 nm.[74,113]

In parallel, evaporation of metal atoms into the low-density supercritical water, as well as penetration of water into the metal layer roughened by the hydrodynamic instability, creates a metal–water mixing region that serves as precursor of the millimeter-sized cavitation bubble expanding on a microsecond time scale. Evaporated metal atoms in the mixing region are the source for nucleation and growth of small (mostly ≤10 nm) particles. Molecular dynamics simulations predicted that the ultrasmall particles (atom clusters) crystallize within a few nanoseconds.[73] Such ultrasmall particles may, under suitable ablation conditions, also be the dominant final product fraction after a single nanosecond laser pulse.[115] However, one may expect that the Rayleigh-instable layer is the main source of yielded nanoparticle mass in ultrashort-pulsed laser ablation.

Zhigilei and co-workers identified another process of large-droplet formation in simulations of ultrashort-pulsed ablation of a silver target submersed in water. Spalled deeper target layers may impact the uppermost molten layer, which induces nanojetting with droplet pinch-off.[73,74] These droplets are partially launched past the low-density mixing region into dense and relatively cold water, where they cool down and solidify within nanoseconds because the temperature is

Figure 5. (a) Evolution of relative particle mass contributions of small (primary, <20 nm) and large silver particles and agglomerates (>20 nm) as derived from time-resolved microspot small-angle x-ray scattering at different heights relative to the flat target surface. Agglomeration is enhanced through the bubble collapse, in particular, close to the target surface.[58] (b) Volume-weighted size histograms of gold particle yield from postmortem analysis by transmission electron microscopy (d_F) and an analytic disc centrifuge (d_H) for laser ablation in liquids in (upper) pure water and (lower) 0.5 mM saline solution (NaCl), showing the quenching effect of a diluted electrolyte solution on nanoparticle concentration.[58,120] (c) Molecular dynamics simulation of the temperature evolution of particles arising from droplet formation during silver ablation in water (1) particle in the dense water phase, (2) at the diffuse boundary of the dense water phase, and (3) in the metal–water mixing region near the hot molten metal). Four time phases with distinct temperature evolution are marked with different colors. (Top and right) The process of crystallization in particle 1 is shown for times between 5300 and 5500 ps (fcc = face-centered cubic, hcp = hexagonally close-packed, and bcc = body-centered cubic). The rapid crystallization leads to small and defect-rich domains.[74] Jetted droplets are quickly cooled and form mismatched or defect-rich solid lattices. The main particle population is trapped inside the bubble and remains in liquid state after a few nanoseconds. (d) Experimental detection of crystalline particles advancing the bubble by recording the scattering intensity, I, as function of scattering angle 2Θ. Larger particles have a narrower angular distribution of scattering intensity than smaller particles. The largest particles are found at the bubble front.[119] (e) Bubble formation by a sequence of two pulses 20 µs apart. Jetted particles from the first pulse may trigger formation of the satellite bubble by the second pulse. The laser-beam path is indicated in red.[74]

below the melting temperature of the metal (Figure 5c). These droplets are predicted to form mismatched or defect-rich solid lattices, whereas large particles trapped in the metal–water mixing region are still in the liquid state after a few nanoseconds and are expected to have a lattice structure with only few defects (inset Figure 5c).[74] Spallation-induced nanojetting is restricted to ultrashort-pulsed laser ablation under stress-confinement conditions.[114,116] However, it is also conceivable that during nanosecond ablation, the generation of large nanoparticles is possible through the decomposition of the molten layer at the ablation plume–water environment interface. It is expected that the mass-dominant particle fraction does not result from jetting, but from metal atom evaporation into the mixing zone and, in particular, from disintegration of the Rayleigh-instable metal layer.

In situ SAXS confirmed that particles around 10 nm already exist early on during the cavitation phase and persist during the bubble motion.[117,118] Only slight growth of these primary particles is seen. Larger particles outside of the plume–water interface (the bubble wall) are observed, by wide-angle x-ray diffraction, to be crystalline (Figure 5d).[119] They are likely the source of smaller adjacent bubbles seen in cavitation bubble imaging experiments (Figure 5e). Further large, secondary particles showing nonspherical, fractal dimensions detected *in situ* during the bubble life cycle probably stem from the bubble shrinking and collapse phase, when the increased mass concentration, pressure, and temperature provide favorable conditions for particle agglomeration (Figure 5a).[117,118] Interestingly, although sonochemical synthesis of nanoparticles mainly relies on the bubble collapse phase, the same event of bubble collapse has been far less investigated in nanoparticle synthesis via LAL.

Linking different nanoparticle species to formation pathways and to different stages of the ablation process and bubble history may have important implications for optimizing the process. In particular, it was demonstrated that addition of monovalent salts quenches the size distribution already inside the bubble vapor,[120] which is explained by stabilization against both primary particle ripening as well as agglomeration. Interestingly, equimolar macromolecular additives do not cause size quenching inside the bubble, and their monomers behave somewhere in between the behavior of anions and polymers.[115]

Nanoparticles produced by LAL undergo oxidation reactions, and when the oxidation happens is still being investigated. Molecular dynamics simulations in literature do not account for chemical reactions, although it is known that laser-generated nanoparticles made of gold are partially oxidized by a few percent, and platinum even by tens of percent of the surface,[26] whereas less noble elements are often totally oxidized. Marzun et al. have shown that nanoparticle oxidation during LAL synthesis is caused mainly by reactive oxygen species originating from decomposition of water molecules, rather than by molecular oxygen.[121] Oxidative species are also known to be created by the laser process itself, as H_2O_2 formation has been found in the colloid.[122] Chemical analysis of the bubble gas composition revealed that water is split into H_2 and O_2.[123] Amans et al. reported for the Al-O system that chemical redox reactions occur in the early phase.[56,124]

Concluding remarks

Ultrasonic sonochemistry and material synthesis through laser ablation in liquids are both inextricably linked with cavitation phenomena. However, while the high temperatures and pressures produced upon bubble collapse are essential for sonochemistry, they promote the aggregation of nanoparticles produced by LAL, which is undesirable. This requires different strategies for the control of collapse conditions in both cases. Increased ambient pressure may enhance the vigor of bubble collapse in ultrasonic cavitation, while appropriate choice of target geometry and liquid viscosity in LALs may enhance the transformation of bubble energy into kinetic energy of a jet flow, which reduces collapse temperature and pressure and promotes mixing.

Hot spots generated during acoustic cavitation can be a powerful tool for the production of nanostructured materials and for modification of existing solids. Ultrasound and cavitation also physically affect an irradiated fluid, causing increased mixing and shearing, heating, shock waves, microjets, and droplet nebulization. These processes can affect reaction rates, crystallization, and particle size. While sonochemistry has been primarily a laboratory tool so far, scaleup of liquid processing with ultrasound has been demonstrated for a variety of processes, even up to 200 m^3/day for sewage sludge treatment.

Material synthesis inside the LAL-bubble has started to be described by molecular dynamics simulation from the early phase until some nanoseconds, and the bubble's interior has been spatiotemporally mapped on the microsecond scale by *in situ* x-ray methods. However, the temporal gap between these two time domains still needs to be filled. Moreover, the influence of the bubble collapse needs to be further explored to complement the information available from *in situ* (bubble) and *ex situ* (colloid) analytical methods.

Today, via LAL, grams of nanoparticles can be produced per hour (equivalent to tens of liters colloid per hour) and downstream-processed into kg of catalyst (e.g., Pt/C[125] or Au/TiO_2[126]) or kg of nanodecorated additive-manufacturing powder (e.g., Ag/polyamide[107] or yttria/steel[108]) per day. Further upscaling will require further advancement of laser technology and bubble dynamics engineering, thus avoiding bubble shielding of the target during LAL. Second, for achieving monodisperse particle populations, size narrowing approaches need to be realized in flow-through processing, such as *in situ* size quenching with graphene yielding high-load, narrow-sized Pt/GNS catalyst in one step (30–40 wt% Pt on C, 2–3-nm size)[127] or liquid-flow downstream laser fragmentation.[128]

Acknowledgments

References

1. W. Lauterborn, T. Kurz, *Rep. Prog. Phys.* **73**, 106501 (2010).
2. C.E. Brennen, *Cavitation and Bubble Dynamics* (Oxford University Press, New York, 1995).
3. A. Vogel, S. Busch, U. Parlitz, *J. Acoust. Soc. Am.* **100**, 148 (1996).
4. A. Vogel, W. Lauterborn, *J. Acoust. Soc. Am.* **84**, 719 (1988).
5. W. Lauterborn, A. Vogel, in *Shock Wave Emission by Laser Generated Bubbles,* C.F. Delale, Ed. (Springer-Verlag, Berlin, 2013), p. 67.
6. T. Prozorov, R. Prozorov, K.S. Suslick, *J. Am. Chem. Soc.* **126**, 13890 (2004).
7. S.J. Doktycz, K.S. Suslick, *Science* **247**, 1067 (1990).
8. J.J. Hinman, K.S. Suslick, *Top. Curr. Chem.* **375**, 1 (2017).
9. A. Vogel, W. Lauterborn, R. Timm, *J. Fluid Mech.* **206**, 299 (1989).
10. A. Philipp, W. Lauterborn, *J. Fluid Mech.* **361**, 75 (1998).
11. M. Dular, T. Pozar, J. Zevnik, R. Petkovsek, *Wear* **418**, 13 (2019).
12. E.A. Brujan, K. Nahen, P. Schmidt, A. Vogel, *J. Fluid Mech.* **433**, 251 (2001).
13. J. Noack, A. Vogel, *IEEE J. Quantum Electron.* **35**, 1156 (1999).
14. B.P. Barber, R.A. Hiller, R. Lofstedt, S.J. Putterman, K.R. Weninger, *Phys. Rep.* **281**, 65 (1997).
15. S.J. Putterman, K.R. Weninger, *Annu. Rev. Fluid Mech.* **32**, 445 (2000).
16. M.P. Brenner, S. Hilgenfeldt, D. Lohse, *Rev. Mod. Phys.* **74**, 425 (2002).
17. K.S. Suslick, D.J. Flannigan, *Annu. Rev. Phys. Chem.* **59**, 659 (2008).
18. E.B. Flint, K.S. Suslick, *Science* **253**, 1397 (1991).
19. D.J. Flannigan, K.S. Suslick, *Nature* **434**, 52 (2005).
20. Y.T. Didenko, K.S. Suslick, *Nature* **418**, 394 (2002).
21. Y.T. Didenko, W.B. McNamara, K.S. Suslick, *Nature* **407**, 877 (2000).
22. Y.T. Didenko, W.B. McNamara, K.S. Suslick, *J. Am. Chem. Soc.* **121**, 5817 (1999).
23. K.S. Suslick, N.C. Eddingsaas, D.J. Flannigan, S.D. Hopkins, H. Xu, *Acc. Chem. Res.* **51**, 2169 (2018).
24. R. Pecha, B. Gompf, *Phys. Rev. Lett.* **84**, 1328 (2000).
25. K.R. Weninger, P.G. Evans, S.J. Putterman, *Phys. Rev. E* **61**, R1020 (2000).
26. D.S. Zhang, B. Goekce, S. Barcikowski, *Chem. Rev.* **117**, 3990 (2017).
27. C. Streich, L. Akkari, C. Decker, J. Bormann, C. Rehbock, A. Muller-Schiffmann, F.C. Niemeyer, L. Nagel-Steger, D. Willbold, B. Sacca, C. Korth, T. Schrader, S. Barcikowski, *ACS Nano* **10**, 7582 (2016).
28. V. Merk, C. Rehbock, F. Becker, U. Hagemann, H. Nienhaus, S. Barcikowski, *Langmuir* **30**, 4213 (2014).
29. T.B. Benjamin, A.T. Ellis, *Philos. Trans. R. Soc. Lond. A* **260**, 221 (1966).
30. A. Vogel, N. Linz, S. Freidank, G. Paltauf, *Phys. Rev. Lett.* **100**, 038102 (2008).
31. B. Han, K. Kohler, K. Jungnickel, R. Mettin, W. Lauterborn, A. Vogel, *J. Fluid Mech.* **771**, 706 (2015).
32. K.R. Weninger, C.G. Camara, S.J. Putterman, *Phys. Rev. E Stat. Nonlin. Soft Matter Phys.* **63**, 016310 (2001).
33. J. Noack, A. Vogel, *Appl. Opt.* **37**, 4092 (1998).
34. A. Vogel, J. Noack, K. Nahen, D. Theisen, S. Busch, U. Parlitz, D.X. Hammer, G.D. Noojin, B.A. Rockwell, R. Birngruber, *Appl. Phys. B* **68**, 271 (1999).
35. G.E. Duvall, G.R. Fowles, in *High Pressure Physics and Chemistry,* R.S. Bradley, Ed. (Academic Press, New York, 1963), p. 209.
36. G.E. Duvall, R.A. Graham, *Rev. Mod. Phys.* **49**, 523 (1977).
37. M. Tinguely, D. Obreschkow, P. Kobel, N. Dorsaz, A. de Bosset, M. Farhat, *Phys. Rev. E* **86**, 046315 (2012).
38. S. Fujikawa, T. Akamatsu, *J. Fluid Mech.* **97**, 481 (1980).
39. I. Akhatov, O. Lindau, A. Topolnikov, R. Mettin, N. Vakhitova, W. Lauterborn, *Phys. Fluids* **13**, 2805 (2001).
40. R. Hickling, M.S. Plesset, *Phys. Fluids* **7**, 7 (1964).
41. M. Koch, C. Lechner, F. Reuter, K. Kohler, R. Mettin, W. Lauterborn, *Comput. Fluids* **126**, 71 (2016).
42. C.P. Lin, M.W. Kelly, *Appl. Phys. Lett.* **72**, 2800 (1998).
43. D. Lapotko, *Opt. Express* **17**, 2538 (2009).
44. A. Siems, S.A.L. Weber, J. Boneberg, A. Plech, *New J. Phys.* **13**, 043018 (2011).
45. V. Kotaidis, A. Plech, *Appl. Phys. Lett.* **87**, 213102 (2005).
46. E. Boulais, R. Lachaine, M. Meunier, *Nano Lett.* **12**, 4763 (2012).
47. R.H. Xiong, K. Raemdonck, K. Peynshaert, I. Lentacker, I. De Cock, J. Demeester, S.C. De Smedt, A.G. Skirtach, K. Braeckmans, *ACS Nano* **8**, 6288 (2014).
48. F. Rudnitzki, S. Feineis, R. Rahmanzadeh, E. Endl, J. Lutz, J. Groll, G. Huttmann, *J. Biophotonics* **11**, 201700329 (2018).
49. C.P. Yao, X.C. Qu, Z.X. Zhang, G. Huttmann, R. Rahmanzadeh, *J. Biomed. Opt.* **14**, 054034 (2009).
50. A. Wilson, J. Mazzaferri, E. Bergeron, S. Patskovsky, P. Marcoux-Valiquette, S. Costantino, P. Sapieha, M. Meunier, *Nano Lett.* **18**, 6981 (2018).
51. A. Plech, S. Ibrahimkutty, S. Reich, G. Newby, *Nanoscale* **9**, 17284 (2017).
52. J. Krawinkel, U. Richter, M.L. Torres-Mapa, M. Westermann, L. Gamrad, C. Rehbock, S. Barcikowski, A. Heisterkamp, *J. Nanobiotechnol.* **14**, 10.1186 (2016).
53. J. Lombard, T. Biben, S. Merabia, *Nanoscale* **8**, 14870 (2016).
54. J. Neumann, R. Brinkmann, *Appl. Phys. Lett.* **93**, 033001 (2008).
55. J. Tomko, J.J. Naddeo, R. Jimenez, Y. Tan, M. Steiner, J.M. Fitz-Gerald, D.M. Bubb, S.M. O'Malley, *Phys. Chem. Chem. Phys.* **17**, 16327 (2015).
56. J. Lam, J. Lombard, C. Dujardin, G. Ledoux, S. Merabia, D. Amans, *Appl. Phys. Lett.* **108**, 074104 (2016).
57. S. Kohsakowski, B. Goekce, R. Tanabe, P. Wagener, A. Plech, Y. Ito, S. Barcikowski, *Phys. Chem. Chem. Phys.* **18**, 16585 (2016).
58. S. Reich, P. Schoenfeld, P. Wagener, A. Letzel, S. Ibrahimkutty, B. Goekce, S. Barcikowski, A. Menzel, T.D. Rolo, A. Plech, *J. Colloid Interface Sci.* **489**, 106 (2017).
59. Q.Y. Zeng, S.R. Gonzalez-Avila, R. Dijkink, P. Koukouvinis, M. Gavaises, C.D. Ohl, *J. Fluid Mech.* **846**, 341 (2018).
60. N. Dabir-Moghaddam, Z. Liu, B.X. Wu, *J. Appl. Phys.* **121**, 044908 (2017).
61. T. Hupfeld, G. Laurens, D. Amans, S. Barcikowski, B. Goekce, "Influence of Wettability and High Viscosity on the Cavitation Bubble Dynamics during Pulsed Laser Ablation in Liquid," in *Proc. 5th Conf. Adv. Nanoparticle Gener. Excitation by Lasers in Liquids,* D. Amans, Ed. (University Lyon, France), p. 15, http://angel-conference.org/en/pages/angel-2018-program.ANGEL 2018 Program, p. 15, http://angel-conference.org/en/pages/angel-2018-program.
62. E. Lauer, X.Y. Hu, S. Hickel, N.A. Adams, *Comput. Fluids* **69**, 1 (2012).
63. C. Lechner, M. Koch, W. Lauterborn, R. Mettin, *J. Acoust. Soc. Am.* **142**, 3649 (2017).
64. W. Lauterborn, C. Lechner, M. Koch, R. Mettin, *IMA J. Appl. Math.* **83**, 556 (2018).
65. A. Vogel, W. Lauterborn, *Appl. Opt.* **27**, 1869 (1988).
66. D. Kroninger, K. Kohler, T. Kurz, W. Lauterborn, *Exp. Fluids* **48**, 395 (2010).
67. F. Reuter, S.R. Gonzalez-Avila, R. Mettin, C.D. Ohl, *Phys. Rev. Fluids* **2**, 064202 (2017).
68. H. Xu, B.W. Zeiger, K.S. Suslick, *Chem. Soc. Rev.* **42**, 2555 (2013).
69. J.H. Bang, K.S. Suslick, *Adv. Mater.* **22**, 1039 (2010).
70. D.G. Shchukin, D. Radziuk, H. Möhwald, *Annu. Rev. Mater. Res.* **40**, 345 (2010).
71. K.S. Suslick, G.J. Price, *Annu. Rev. Mater. Res.* **29**, 295 (1999).
72. H. Xu, N.C. Eddingsaas, K.S. Suslick, *J. Am. Chem. Soc.* **131**, 6060 (2009).
73. C.Y. Shih, M.V. Shugaev, C.P. Wu, L.V. Zhigilei, *J. Phys. Chem. C* **121**, 16549 (2017).
74. C.Y. Shih, R. Streubel, J. Heberle, A. Letzel, M.V. Shugaev, C.P. Wu, M. Schmidt, B. Goekce, S. Barcikowski, L.V. Zhigilei, *Nanoscale* **10**, 6900 (2018).
75. K.S. Suslick, S.B. Choe, A.A. Cichowlas, M.W. Grinstaff, *Nature* **353**, 414 (1991).
76. D.J. Flannigan, S.D. Hopkins, K.S. Suslick, *J. Organomet. Chem.* **690**, 3513 (2005).
77. J.D. Oxley, T. Prozorov, K.S. Suslick, *J. Am. Chem. Soc.* **125**, 11138 (2003).
78. K.S. Suslick, M. Fang, T. Hyeon, *J. Am. Chem. Soc.* **118**, 11960 (1996).
79. M.W. Grinstaff, A.A. Cichowlas, S.B. Choe, K.S. Suslick, *Ultrasonics* **30**, 168 (1992).
80. M.M. Mdleleni, T. Hyeon, K.S. Suslick, *J. Am. Chem. Soc.* **120**, 6189 (1998).
81. T. Hyeon, M. Fang, K.S. Suslick, *J. Am. Chem. Soc.* **118**, 5492 (1996).
82. C. Cau, S.I. Nikitenko, *Ultrason. Sonochem.* **19**, 498 (2012).
83. C.L. Baigent, G. Müller, *Experientia* **36**, 472 (1980).
84. M.A. Alavi, A. Morsali, *Ultrason. Sonochem.* **17**, 441 (2010).
85. M.A. Alavi, A. Morsali, *Ultrason. Sonochem.* **17**, 132 (2010).
86. M. Salavati-Niasari, J. Javidi, F. Davar, *Ultrason. Sonochem.* **17**, 870 (2010).
87. D. Ghanbari, M. Salavati-Niasari, M. Ghasemi-Kooch, *J. Ind. Eng. Chem.* **20**, 3970 (2014).
88. A.P. Nagvenkar, A. Deokar, I. Perelshtein, A. Gedanken, *J. Mater. Chem. B* **4**, 2124 (2016).
89. P.K. Vabbina, A. Kaushik, N. Pokhrel, S. Bhansali, N. Pala, *Biosens. Bioelectron.* **63**, 124 (2015).
90. G. Singh, E.M. Joyce, J. Beddow, T. J Mason, *J. Microbiol. Biotechnol. Food Sci.* **2**, 106 (2012).
91. R. Gottesman, S. Shukla, N. Perkas, L.A. Solovyov, Y. Nitzan, A. Gedanken, *Langmuir* **27**, 720 (2011).
92. A. Abramova, A. Gedanken, V. Popov, E.-H. Ooi, T.J. Mason, E.M. Joyce, J. Beddow, I. Perelshtein, V. Bayazitov, *Mater. Lett.* **96**, 121 (2013).
93. N.K. Neelakantan, P.B. Weisensee, J.W. Overcash, E.J. Torrealba, W.P. King, K.S. Suslick, *RSC Adv.* **5**, 69243 (2015).
94. S.E. Skrabalak, *Phys. Chem. Chem. Phys.* **11**, 4930 (2009).
95. J. Guo, S. Zhu, Z. Chen, Y. Li, Z. Yu, Q. Liu, J. Li, C. Feng, D. Zhang, *Ultrason. Sonochem.* **18**, 1082 (2011).
96. Y. Cui, D. Zhou, Z. Sui, B. Han, *Chin. J. Chem.* **33**, 119 (2014).
97. S. Zhu, J. Guo, J. Dong, Z. Cui, T. Lu, C. Zhu, D. Zhang, J. Ma, *Ultrason. Sonochem.* **20**, 872 (2013).
98. K. Krishnamoorthy, G.-S. Kim, S.J. Kim, *Ultrason. Sonochem.* **20**, 644 (2013).

99. H. Xu, K.S. Suslick, *J. Am. Chem. Soc.* **133**, 9148 (2011).
100. S.-H. Jeong, J.-H. Ko, J.-B. Park, W. Park, *J. Am. Chem. Soc.* **126**, 15982 (2004).
101. H. Ha, S.-H. Jeong, *Korean J. Chem. Eng.* **33**, 401 (2016).
102. K. Wei, J. Li, Z. Ge, Y. You, H. Xu, *RSC Adv.* **4**, 52230 (2014).
103. C. Rehbock, J. Jakobi, L. Gamrad, S. van der Meer, D. Tiedemann, U. Taylor, W. Kues, D. Rath, S. Barcikowski, *Beilstein J. Nanotechnol.* **5**, 1523 (2014).
104. D.S. Zhang, J. Liu, P.F. Li, Z.F. Tian, C.H. Liang, *ChemNanoMat* **3**, 512 (2017).
105. R. Streubel, S. Barcikowski, B. Goekce, *Opt. Lett.* **41**, 1486 (2016).
106. S. Jendrzej, B. Gokce, M. Epple, S. Barcikowski, *ChemPhysChem* **18**, 1012 (2017).
107. T. Hupfeld, T. Laumer, T. Stichel, T. Schuffenhauer, J. Heberle, M. Schmidt, S. Barcikowski, B. Goekce, *Procedia CIRP* **74**, 244 (2018).
108. C. Donate-Buendia, F. Fromel, M.B. Wilms, R. Streubel, J. Tenkamp, T. Hupfeld, M. Nachev, E. Goekce, A. Weisheit, S. Barcikowski, F. Walther, J.H. Schleifenbaum, B. Goekce, *Mater. Des.* **154**, 360 (2018).
109. D.S. Zhang, J. Liu, C.H. Liang, *Sci. China Phys. Mech.* **60**, 074201 (2017).
110. S. Ibrahimkutty, P. Wagener, T.D. Rolo, D. Karpov, A. Menzel, T. Baumbach, S. Barcikowski, A. Plech, *Sci. Rep.* **5**, 16313 (2015).
111. S. Kohsakowski, A. Santagata, M. Dell'Aglio, A. de Giacomo, S. Barcikowski, P. Wagener, B. Goekce, *Appl. Surf. Sci.* **403**, 487 (2017).
112. S. Reich, J. Goettlicher, A. Letzel, B. Goekce, S. Barcikowski, T. dos Santos Rolo, T. Baumbach, A. Plech, *Appl. Phys. A* **124**, 71, (2018), doi:10.1007/s00339.
113. C.Y. Shih, C.P. Wu, M.V. Shugaev, L.V. Zhigilei, *J. Colloid Interface Sci.* **489**, 3 (2017).
114. A. Vogel, V. Venugopalan, *Chem. Rev.* **103**, 577 (2003).
115. A. Letzel, S. Reich, T. dos Santos Rolo, A. Kanitz, J. Hoppius, A. Rack, M. Olbinado, A. Ostendorf, B. Goekce, A. Plech, S. Barcikowski, *Langmuir* **35**, 3038 (2019).
116. L.V. Zhigilei, E. Leveugle, B.J. Garrison, Y.G. Yingling, M.I. Zeifman, *Chem. Rev.* **103**, 321 (2003).
117. S. Ibrahimkutty, P. Wagener, A. Menzel, A. Plech, S. Barcikowski, *Appl. Phys. Lett.* **101**, 103104 (2012).
118. P. Wagener, S. Ibrahimkutty, A. Menzel, A. Plech, S. Barcikowski, *Phys. Chem. Chem. Phys.* **15**, 3068 (2013).
119. S. Reich, A. Letzel, A. Menzel, N. Kretschmar, B. Goekce, S. Barcikowski, A. Plech, *Nanoscale* **11**, 6962 (2019).
120. A. Letzel, B. Goekce, P. Wagener, S. Ibrahimkutty, A. Menzel, A. Plech, S. Barcikowski, *J. Phys. Chem. C* **121**, 5356 (2017).
121. G. Marzun, H. Bonnemann, C. Lehmann, B. Spliethoff, C. Weidenthaler, S. Barcikowski, *ChemPhysChem* **18**, 1175 (2017).
122. E.V. Barmina, S.V. Gudkov, A.V. Simakin, G.A. Shafeev, *J. Laser Micro/Nanoeng.* **12**, 254 (2017).
123. M.R. Kalus, N. Barsch, R. Streubel, E. Goekce, S. Barcikowski, B. Goekce, *Phys. Chem. Chem. Phys.* **19**, 7112 (2017).
124. J. Lam, D. Amans, F. Chaput, M. Diouf, G. Ledoux, N. Mary, K. Masenelli-Varlot, V. Motto-Ros, C. Dujardin, *Phys. Chem. Chem. Phys.* **16**, 963 (2014).
125. S. Kohsakowski, R. Streubel, I. Radev, V. Peinecke, S. Barcikowski, G. Marzun, S. Reichenberger, *Appl. Surf. Sci.* **467**, 486 (2019).
126. W.W. Dong, S. Reichenberger, S. Chu, P. Weide, H. Ruland, S. Barcikowski, P. Wagener, M. Muhler, *J. Catal.* **330**, 497 (2015).
127. I. Haxhiaj, S. Tigges, D. Firla, X.R. Zhang, U. Hagemann, T. Kondo, J. Nakamura, G. Marzun, S. Barcikowski, *Appl. Surf. Sci.* **469**, 811 (2019).
128. F. Waag, B. Goekce, C. Kalapu, G. Bendt, S. Salamon, J. Landers, U. Hagemann, M. Heidelmann, S. Schulz, H. Wende, N. Hartmann, M. Behrens, S. Barcikowski, *Sci. Rep.* **7**, 13161 (2017). ☐

Stephan Barcikowski is the chair of the Institute of Technical Chemistry I at the University of Duisburg-Essen, Germany, and is scientific director of the Center for Nanointegration Duisburg-Essen CENIDE, Germany. He studied chemistry at Technical University Braunschweig and Leibniz University Hannover, Germany, where he earned his PhD degree in mechanical engineering (materials). He has more than 180 reviewed papers and patent files. He launched the scientific video channel "Nanofunction" on YouTube with more than 11,000 annual visits, co-founded the company Particular GmbH, and is an editor of *Applied Surface Science*. Barcikowski can be reached by email at stephan.barcikowski@uni-due.de.

Anton Plech is a senior scientist at the Karlsruhe Institute of Technology, Germany, and a lecturer at Konstanz University, Germany. He received his PhD degree in physics at the Ludwig Maximilian University of Munich, Germany, in 2000, and Habilitation degree at Konstanz University in 2007. His research interests include static and dynamic analysis of materials structure and structure formation with emphasis on the nanoscale, phase transitions, and light–matter interactions. Plech can be reached by email at anton.plech@kit.edu.
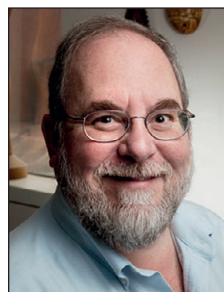
Kenneth S. Suslick is the Schmidt Research Professor of Chemistry at the University of Illinois at Urbana-Champaign, and for 2018–2019, the Eastman Professor at the University of Oxford, UK. He received his BS degree from the California Institute of Technology in 1974 and his PhD degree from Stanford University in 1978. He is the recipient of the Materials Research Society (MRS) Medal, Centenary Prize, and Sir George Stokes Medal of the Royal Society of Chemistry (RSC), ACS Nobel Laureate Signature Award, American Chemical Society (ACS) Senior Cope Scholar Award, and Acoustical Society of America (ASA) Helmholtz-Rayleigh Interdisciplinary Silver Medal. He is a Fellow of the AAAS, ACS, RSC, MRS, American Physical Society, ASA, and the National Academy of Inventors. He has published more than 400 papers, edited four books, and holds 42 patents. Suslick can be reached by email at ksuslick@illinois.edu.

Alfred Vogel is a full professor and director of the Institute of Biomedical Optics at the University of Luebeck, Germany, Deputy CEO of the Medical Laser Center at the University of Luebeck GmbH, and adjunct professor at Xi'an Jiaotong University, China. He received his PhD degree in physics from the University of Göttingen, Germany, in 1987. He is a Fellow of the International Society for Optics and Photonics (SPIE), and The Optical Society (OSA), an editorial board member for the *Journal of Biomedical Optics*, advisory editor of *Biomedical Optics Express*, and was an associate editor of *Optics Express*. His research interests include pulsed and plasma-mediated laser interactions with water, cells, and biological tissues. Vogel can be reached by email at vogel@bmo.uni-luebeck.de.